THE JOURNAL OF PHYSICAL CHEMISTRY A

Article

pubs.acs.org/JPCA

Effects of High Angular Momentum on the Unimolecular Dissociation of CD_2CD_2OH: Theory and Comparisons with Experiment

Benjamin G. McKown,[†] Michele Ceriotti,[‡] Caroline C. Womack,[†] Eugene Kamarchik,[§] Laurie J. Butler,*[,†] and Joel M. Bowman[∥]

[†]Department of Chemistry and the James Franck Institute, University of Chicago, Chicago, Illinois 60637, United States

[‡]Institute of Materials, École Polytechnique Fédérale de Lausanne (EPFL), CH-1015 Lausanne, Switzerland

[§]Combustion Research Facility, Sandia National Laboratories, Livermore, California 94551, United States

[∥]Cherry L. Emerson Center for Scientific Computation, Department of Chemistry, Emory University, Atlanta, Georgia 30322, United States

Supporting Information

ABSTRACT: This paper explores the dynamics of a highly rotationally and vibrationally excited radical, CD_2CD_2OH. The radical is produced from the 193 nm photodissociation of 2-bromoethanol-d_4, so it is imparted with high angular momentum and high vibrational energy and subsequently dissociates to several product channels. This paper focuses on characterizing its angular momentum and modeling its effect on the product channels, including the HOD + vinyl-d_3 product channel resulting from a frustrated dissociation of the radical originally en route to OH + ethene-d_4 that instead results in D atom abstraction. Our impulsive model of the initial photodissociation shows that, for some cases, upward of 200 au of angular momentum is imparted, which greatly affects the dynamics of the competing product channels. Using a permutationally invariant potential energy surface and quasiclassical trajectories, we simulated the dissociation dynamics of CD_2CD_2OH and compared these results to those of Kamarchik et al. (*J. Phys. Chem. Lett.* **2010**, *1*, 3058−3065), who studied the dynamics of CH_2CH_2OH with zero angular momentum. We found that the recoil translational energy distribution for radicals that dissociated to OH + C_2D_4 matched experiment closely only when high angular momentum of the initial radical was explicitly included in the trajectory calculations. Similarly, the rate constant for dissociation changes when rotational energy was added to the vibrational energy in the initial conditions. Lastly, we applied the sketch-map dimensionality reduction technique to analyze mechanistic information leading to the vinyl + water product channel. Projecting the ab initio intrinsic reaction coordinates onto the lower dimensional space identified with sketch map offers new insight into the dynamics when one looks at the simulated trajectories in the lower dimensional space. Further analysis shows that the transition path resembles a frustrated dissociation of the OH + ethene radical adduct, followed instead by branching to vinyl + water when the leaving OH group encounters a nearby D atom on the ethene moiety. This characterization is in accord with the one made previously. We show that the transition path bifurcation between the two similar channels occurs at carbon−oxygen distances and oxygen-abstracted deuterium distances of 2−2.5 Å controlled by the C−O−D bond angle with large angles preferentially branching to the water plus vinyl product state. The experimental branching ratios were not reproduced by theory, however, due partly to the insufficient quality of the fitted potential surface. We also have evidence of a minor product channel, HD + vinoxy-d_3, from our molecular dynamics simulations that allows us to assign the HD signal in prior experimental work.

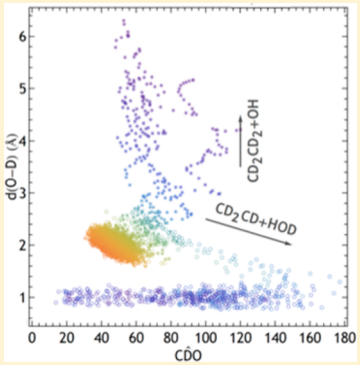

INTRODUCTION

The unimolecular and bimolecular reactions that control atmospheric and combustion chemistry typically involve highly vibrationally excited radical intermediates. Even small radicals (8−12 atoms) have high dimensionality potential energy surfaces (PESs) that can result in numerous competing chemical reaction product channels. Recently, the study of the β-hydroxyethyl radical (CH_2CH_2OH) has been undertaken by many groups, using various theoretical and experimental means, building on kinetics measurements of the OH + ethene reaction.[1−15] This radical has been studied extensively because it represents the main addition adduct of the bimolecular collision between the hydroxyl radical and ethene, the simplest unsaturated hydrocarbon in the atmosphere. At high temperatures, early work concluded that hydroxyl radical reacts with ethene by abstracting one of the four equivalent hydrogen atoms, producing water and vinyl radical (R1), while at low temperatures the hydroxyl radical can add directly to the double

Received: August 7, 2013
Revised: September 20, 2013
Published: October 14, 2013

bond of C_2H_4 forming the β-hydroxyethyl radical (R2). The addition product, CH_2CH_2OH, is formed with no potential barrier and is ~18 kcal mol^{-1} below the H_2O plus vinyl product asymptote.

$$C_2H_4 + OH \rightarrow H_2O + C_2H_3 \quad (R1)$$

$$C_2H_4 + OH \rightarrow CH_2CH_2OH \quad (R2)$$

In a bulk gas-phase experiment, if the CH_2CH_2OH addition product does not suffer many inelastic collisions, it can retain enough internal energy to dissociate either to OH + ethene or to several other competing product channels. We thus undertook a multiyear investigation of the unimolecular dissociation dynamics of CH_2CH_2OH starting from the brominated precursor, 2-bromoethanol. Klippenstein and co-workers previously calculated the stationary points on the potential surface of C_2H_5O at the RQCISD(T)/cc-pV∞Z//UQCISD/6-311++G(d,p) level of theory which clearly showed that the lowest barrier corresponds to dissociation to OH + ethene via a slightly stabilized, hydrogen bonded complex where the OH hydrogen is attracted to the partially negative region of ethene's π-cloud.[12] From there, the weakly bound system can break free from the electron-rich ethene to fully dissociate, or it can abstract one of the four hydrogens from ethene. The first process is lower in energy by approximately 6 kcal mol^{-1}; therefore, almost all nascent radicals should preferentially dissociate to this lower energy channel. However, after probing this system experimentally, we reported roughly 14% branching to the water plus vinyl channel—quite a surprising result which disagrees with RRKM predictions of less than 1%.[16,17] As with many reactions involving hydrogen, this large, unexpected contribution was originally attributed to tunneling effects. To investigate further, a similar study of the deuterated precursor, 2-bromoethanol-d_4 ($BrCD_2CD_2OH$), was undertaken. If dominated by tunneling, the branching fraction to the water plus vinyl channel would be expected to decrease for the deuterated precursor. Somewhat surprisingly, however, the branching was similar, roughly 20% of the total product signal.[18,19]

Since tunneling effects were effectively ruled out because the branching to water + vinyl did not decrease, we are re-examining our analysis of the system. When the photo-dissociation event occurs, the repulsive force between the bromine atom and the carbon atom in the radical moiety impacts far from the radical fragment's center of mass. This causes the radical to rotate, so the radical is formed with a large fraction of its total internal energy stored in rotational motion. Therefore, the vibrational energy, which in a simple treatment might be assumed to be the only "usable" energy to surmount dissociation and isomerization barriers, is lowered considerably. In a more detailed treatment, one recognizes that it is not rotational energy that is conserved during the dynamics but rather angular momentum. Similarly, the added constraint of high angular momentum (high J) can drastically change the effective potential landscape when one adds the rotational energy, which changes the relative energetics of barriers en route to the product channels. We recently developed an impulsive model to predict rotational energy partitioning based on the experimentally derived translational energy distribution of the departing halogen atom.[18] This model is refined here to include the full inertia tensor of the dissociating radical species.

In 2010, Kamarchik et al. reported a permutationally invariant potential energy surface to study CH_2CH_2OH and its various isomers and product channels using quasiclassical trajectories.[20] The surface was formed by fitting over 50 000 ab initio data points at B3LYP/cc-pVDZ and CCSD/cc-pVDZ levels of theory to a permutationally invariant polynomial basis. While for most geometries B3LYP provided an adequate estimate of the potential, the stationary points on the PES were calculated using CCSD/cc-pVDZ yielding higher accuracy near those points. The main results reported show an unexpected "roaming" pathway leading to water and vinyl radical—very similar to our experimental studies. Although this PES does not fully reproduce the experimental results, giving only a 1% branching to the water plus vinyl pathway, we believe it still captures many of the underlying physics in the dissociation process. In order to more accurately model the conditions of our experiments, we have undertaken a similar study. In contrast to their $J = 0$ au study, where the angular momentum was explicitly removed, we ran a series of trajectories with angular momentum determined by our impulsive model. Not only would these trajectories be a better model of our experimental conditions but also we expected that the addition of rotational energy might change the relative energies on the effective PES thus leading to a higher water plus vinyl branching fraction.

Much work has been done in past years to understand the mechanistic motions leading to roaming pathways and frustrated dissociations. Bowman and co-workers have done important work in this area, mainly focusing on identifying closed-shell and radical systems with large contributions from roaming pathways, such as hydrogen formation from formaldehyde.[21] For some systems, they have determined that the departing fragment must depart sufficiently slowly to be "trapped" on a flat portion of the potential energy surface, allowing the two fragments to sample a large number of relative orientations until the two either completely separate or a lower energy pathway is found resulting in new product formation. Traditional transition-state theories (e.g., RRKM) cannot adequately model such a process; even steepest descent transition-state searches fail to properly classify transition states as many of these roaming pathways represent bifurcations in phase space.[22,23] Due to the complexity of such processes, new techniques must be used to analyze the molecular dynamics data.

The scientific community has increasingly been relying on atomistic simulations to uncover underlying dynamics and mechanistic motions explaining various chemical phenomena. However, understanding such data usually requires keen chemical intuition and years of experience. Although visualizing the trajectories yields excellent information, it becomes intractable, as many thousands of trajectories are required to uncover statistical properties. Additionally, as the complexity of the systems increases, dimensionality reduction techniques become increasingly important to analyze the data sets recovered from trajectory simulations. These methods have been applied to vastly different systems with varied success depending on technique and molecular process. Largely, these methods can be classified as either linear or nonlinear. Linear techniques require the relevant underlying data set (d-dimensional) to lie on a linear subspace of the full (D-dimensional) space (i.e., the subspace is a Euclidean space in d-dimensions). The most commonly used linear reduction technique is principal component analysis where the principal components are given by the eigenvectors corresponding to the largest eigenvalues of the covariance matrix, themselves being

linear combinations of the initial coordinates (normal modes, interatomic distances, and Cartesian coordinates, etc.). Nonlinear manifold learning techniques do not require that the important data set lie on a Euclidean subspace; however, the data set is assumed to lie on a manifold in d-dimensions of the D-dimensional space. The requirement here is not that the subspace globally represents Euclidian space, as is demanded in linear reduction techniques, but that the subspace locally appears as Euclidean space such that each data point is surrounded by some neighborhood of points that is essentially linear. Examples of nonlinear methods are Isomap,[24,25] metric multidimensional scaling,[26] and diffusion map,[27−30] of which diffusion map has shown the most promise as it is the most robust to noise and applicable to many different processes.

There are several challenges associated with dimensionality reduction methods when applied to atomistic simulations. The methods described above require that the subspace lie on a global Euclidian surface or one that locally transforms as Euclidian space for some neighborhood of points surrounding each point of interest. These requirements are hard to reconcile with some aspects of chemical motion. In fact, the vibrational motion of the molecule associated with thermal fluctuations is intrinsically high dimensional and leads to heavy sampling of the wells on the potential surface. As the molecule follows a transition pathway from one well to another, the sampling of data points is poor compared to the longer time fluctuations within the basin. The poor sampling buries the important reaction pathways connecting one basin to the next, making it difficult to uncover the underlying dynamics.

Sketch map, a new method introduced by Ceriotti et al.,[31−33] was developed specifically to deal with large dimensional data sets from molecular dynamics trajectories and to combat the problems listed previously. This technique has recently been applied to study the complicated free energy surfaces (FES) of polyalanine-12, as well as the structures of both 38 atom and 55 atom Lennard-Jones clusters with much success. In this paper, we apply sketch map to uncover mechanistic information about the dissociation of CD_2CD_2OH to form vinyl (C_2D_3) and water (HOD). We show that sketch map can be a powerful method to uncover dynamic processes of small molecules of atmospheric importance and used to understand novel reaction mechanisms. Similarly, we have used this technique in conjunction with ab initio calculations of the stable points and intrinsic reaction coordinates (IRCs) associated with all pertinent product channels by projecting these calculated structures in the lower dimensional space and analyzing the mapping to uncover the pertinent dynamics.

THEORETICAL METHODS

a. Impulsive Model for Rotational Energy Partitioning. We have previously introduced a modified impulsive model to approximate the fraction of the internal energy in the nascent radicals that is partitioned into rotational instead of vibrational degrees of freedom.[16,34] This model is based on conservation of angular momentum during the photodissociation event and uses the fact that the precursor molecule has been rotationally cooled in the supersonic expansion of a molecular beam such that the total angular momentum prior to its photodissociation is zero; the total angular momentum of the photofragments following the dissociation must therefore also be zero. Hence the vector sum of the orbital angular momentum of the two fragments and the internal rotational angular momentum of the two polyatomic fragments must be the null vector. Note in the present case when one fragment is an atom the sum of the orbital and polyatomic fragment sum to zero. Orbital angular momentum is defined as $\vec{J}_{orb} = \vec{r} \times \vec{p}$, where $\vec{r}$ is the vector between the centers of mass of the departing fragments and $\vec{p}$ is the linear momentum vector. Here, $\vec{p}$ is assumed to be aligned along the breaking bond and has a magnitude proportional to the experimentally measured relative velocity. The rotational angular momentum is given by $\vec{J}_{rot} = \mathbf{I}\vec{\omega}$, where $\mathbf{I}$ is the inertia tensor of the polyatomic radical and $\vec{\omega}$ is the angular velocity vector which defines the axis of rotation.

The classical expression for rotational energy is $E_{rot} = (1/2)\vec{\omega}^T\vec{J}_{rot}$. Solving the expression for $\vec{J}_{rot}$ in terms of $\vec{\omega}^T$ and inserting it into the above equation yield the expression $E_{rot} = (1/2)\vec{J}_{rot}^T\,\mathbf{I}^{-1}\vec{J}_{rot}$. Early classic models for energy partitioning in photodissociation[35−38] implicitly assumed that the rotation takes place about one of three principal axes of rotation defined by the eigenvectors of the inertia tensor. In that case, ω has only one nonzero component, $\mathbf{I}$ is a diagonal matrix, and J is parallel to ω; thus, E_{rot} simplifies to $(1/2)J^2/I$, where I is one of the scalar diagonal entries in the matrix. This expression is typically reported as the definition of rotational energy; however, when the radical is rotating about some arbitrary axis of rotation, such as the rotation being generated by an impulsive dissociation of the C−Br bond in the photolytic precursor generating the radical, the general expression for E_{rot} should be used. In particular, we may substitute the definition of $-\vec{J}_{orb}$ for $\vec{J}_{rot}$ to obtain a definition of E_{rot} that is dependent on the geometry of the parent molecule and the experimentally determined recoil velocity between the halogen and the radical:

$$E_{rot} = \frac{1}{2}(\vec{r} \times \mu\vec{v}_{rel})^T\mathbf{I}^{-1}(\vec{r} \times \mu\vec{v}_{rel}) \tag{1.1}$$

In this equation, $\mathbf{I}^{-1}$ is the inverse of the inertia tensor and is not a scalar.

From eq 1.1 it can be seen that rotational energy can be derived from the Cartesian coordinates of the precursor molecule, with $\vec{J}$ perpendicular to the plane defined by the atom centers in the impulsively breaking C−Br bond (which gives the direction of the relative velocity vector) and the center of mass of the radical fragment in the precursor. However, our model also takes the additional step of considering the full range of parent molecule geometric configurations as it vibrates along its zero-point motion associated with the C−C−Br bending mode. Each configuration of the parent molecule will generate a slightly different amount of rotational energy, and our model adjusts the prediction accordingly. The model also considers how the rotational energy imparted to the radical during the photodissociation is changed as the radical undergoes subsequent dynamics, so its inertia tensor changes. In our prior study,[19] we photodissociated 2-bromoethanol-d_4 and measured the kinetic energy distribution imparted to the Br and CD_2CD_2OH radical fragments. We used the above model, but with $\mathbf{I}$ approximated by a scalar value, to estimate how that photodissociation (in which the parent molecule was excited to a highly repulsive state) imparted a large amount of rotational energy to the nascent radicals. In the same paper, we described how this rotational energy might influence the subsequent relative branching ratio between the OH + ethene dissociation channel and the H-abstraction channel to water + vinyl. We improve on that analysis herein using the full inertia tensor.

Figure 1 shows the distribution of $J = |\vec{J}|$ values of the radical, calculated using the experimental distribution of recoil

dx.doi.org/10.1021/jp407913t | J. Phys. Chem. A 2013, 117, 10951−10963

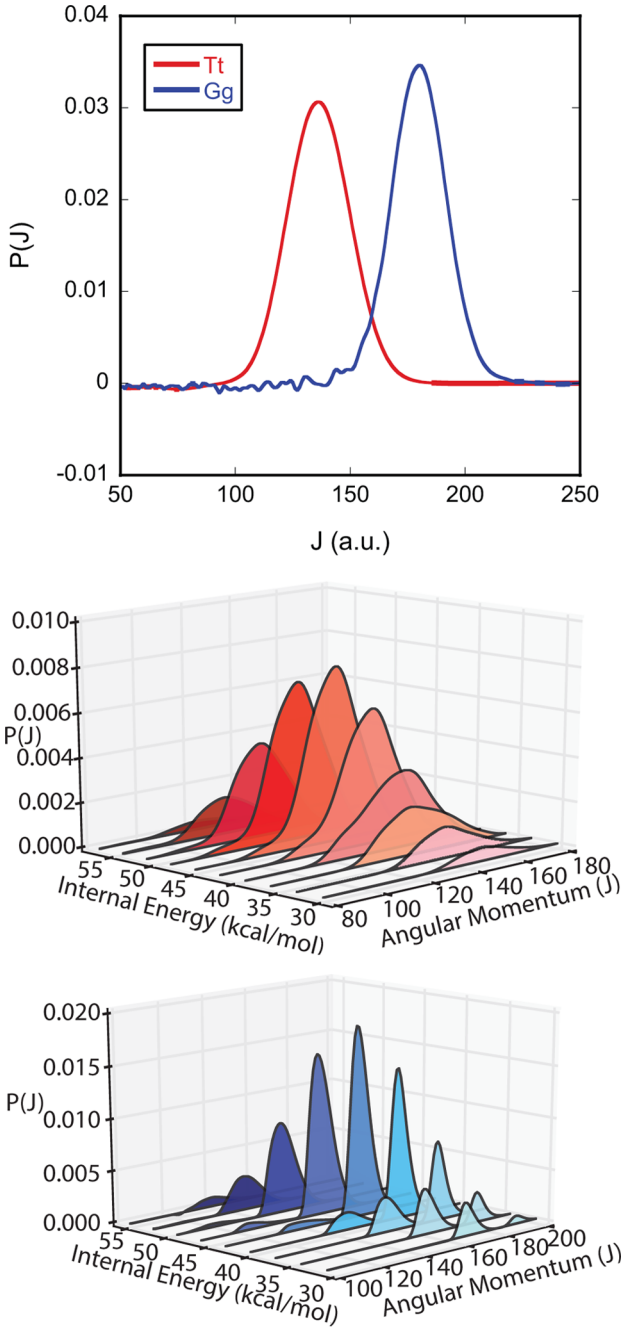

Figure 1. (Top) Calculated $P(J)$ for CD_2CD_2OH radicals generated by the photodissociation of 2-bromoethanol-d_4 in the Tt (red) and Gg (blue) conformers. The distributions peak at 139 and 180 au, respectively, indicating that a large rotational energy is imparted to the nascent fragments. The distributions are convolved over all precursor geometries along the C−C−Br bending mode, all possible internal energies of the parent molecule, and all possible translational energies from the experimentally determined distribution, as well as the $^2P_{3/2}$ and $^2P_{1/2}$ spin−orbit states of the departing Br fragment. (Bottom two frames) show slices of the distribution along certain internal energies of the radical, the red distribution corresponding to radicals dissociating from the Tt conformation of 2-bromoethanol-d_4 and the blue for the Gg conformation. The Supporting Information shows the distribution of J's imparted to the radical when the Tt conformer and the Gg conformer dissociate and partition 32 kcal mol^{-1} to relative kinetic energy, distinguishing the radicals formed in conjunction with Br($^2P_{3/2}$) vs Br($^2P_{1/2}$).

translational energies and accounting for the full range of the C−C−Br bending motion in both the Tt (trans) and Gg (gauche) conformers of the parent molecule. One can see that the distributions peak at 136 and 180 au for the respective conformers, indicating that a great deal of angular momentum was imparted to the radicals. Free from external forces, angular momentum will remain constant, and rotational energy will adjust according to the inertia tensor while the total rotational + vibrational + potential energy stays constant. At any geometry on the potential energy surface we can calculate how the rotational energy has changed. Then, if we add the resulting required rotational energy to each potential energy along, say, the intrinsic reaction coordinate, we generate an effective potential energy along the IRC. Figure 2 shows an example of the effect of large J on two IRCs.

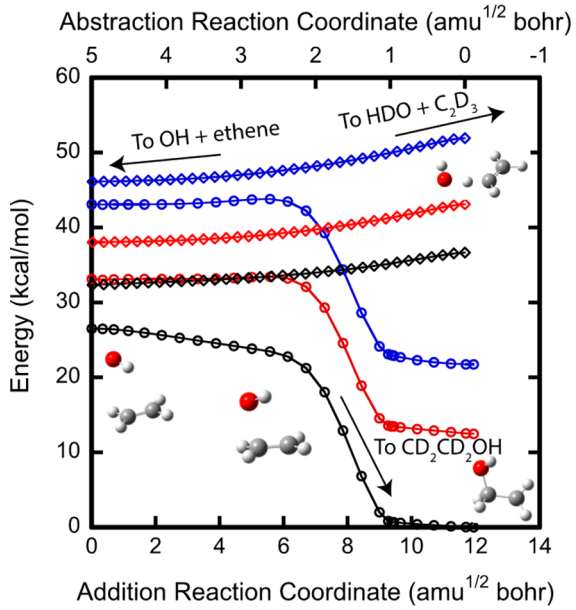

Figure 2. Intrinsic reaction coordinates for the dissociation of CD_2CD_2OH to OH + C_2D_4 (circles) and the H-abstraction pathway leading from OH + C_2D_4 to HDO + C_2D_3 (diamonds). The black traces show the uncorrected IRC, calculated at the B3LYP/6-311++G(3df,2p) level of theory. The red and blue traces have been centrifugally corrected to account for the rotation of the nascent radicals formed from the Tt (red), J = 127 au., and Gg (blue), J = 175 au, conformers. This correction was obtained by calculating the moment of inertia tensor at each geometry along the reaction coordinate, using eq 1.1 to calculate how the rotational energy has changed, and adding that rotational energy to the uncorrected trace. It can be seen that the energy difference between the two transition states in the uncorrected reaction coordinates is over 5 kcal mol^{-1}, but it decreases to less than 2 kcal mol^{-1} in the blue trace, indicating that the large amount of rotational energy in the radicals causes the H-abstraction pathway to be more likely.

b. Classical Trajectories. Permutationally invariant potential energy surfaces used with quasiclassical trajectory simulations have been employed recently with success to model the dynamics of small molecules such as CH_5^+, CH_2O, and H_5^+.[39−42] The C_2H_5O potential surface used here was created[20] by fitting over 50 000 ab initio data points to a permutationally invariant polynomial basis using B3LYP/cc-pVDZ for the majority of data points and CCSD/cc-pVDZ for those geometries in the vicinity of stationary points. The robustness of the surface was checked for reproducibility of all stable

dx.doi.org/10.1021/jp407913t | J. Phys. Chem. A 2013, 117, 10951−10963

minima and transition states of interest; similarly, the curvatures of the reaction paths were analyzed for accuracy. Although the surface is not accurate enough to reproduce experimental branching ratios, qualitative results regarding kinetic and dynamic information can be extracted.

The initial conditions of the simulations were chosen in line with the experimental conditions.[19] The portion of the C−Br photofission $P(E_T)$ that produces radicals with enough internal energy to surmount reaction barriers is shown in Figure 3. We

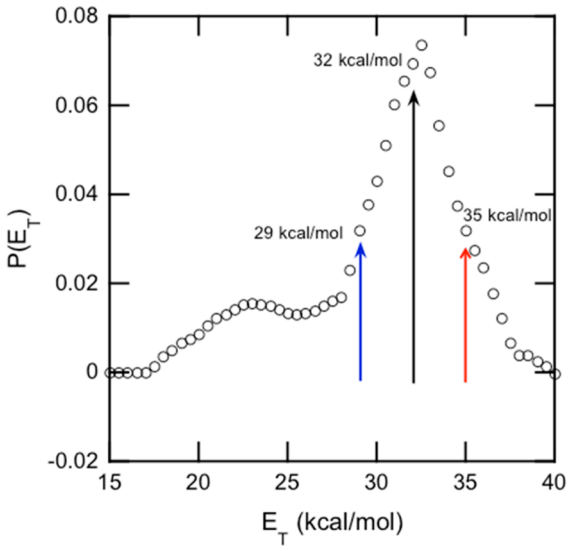

Figure 3. Portion of the experimentally measured translational energy distribution, calculated from the data in ref 19, which produces radicals with enough internal energy to dissociate (series of black circles). The three initial conditions chosen for the simulations are shown by the three arrows: the blue arrow corresponding to 29 kcal mol^{-1} in translation, the black to 32 kcal mol^{-1}, and the red to 35 kcal mol^{-1}.

chose three representative recoil translational energies between the Br and CD_2CD_2OH fragment equally spaced along the distribution. The angular momentum distributions were then determined for all translational energies sampled. We limited our investigation to radicals produced from the photodissociation of two representative conformers of 2-bromoethanol-d_4, a trans conformer (Tt) and a gauche conformer (Gg). Given that each recoil translational energy along the $P(E_T)$ has a corresponding distribution of angular momenta $P(J)$, any attempt to sample all combinations of translational energy and angular momentum would simply be intractable. Therefore, a representative angular momentum was chosen from each $P(J)$ for each E_T and precursor geometry. These initial conditions were chosen as input for our simulations (see Table 1). Given the E_T and angular momentum, the rotational energy was subsequently determined, with the remaining total energy

Table 1. Initial Conditions for All Classical Trajectories Simulations Sorted by Conformer and Recoil Translational Energy between the Br Atom and 2-Hydroxyethyl-d_4

	Tt conformer		Gg conformer	
E_T (kcal mol^{-1})	E_{int} (kcal mol^{-1})	J (au)	E_{int} (kcal mol^{-1})	J (au)
29.0	50.8	127.0	49.3	166.9
32.0	47.8	133.4	46.3	175.3
35.0	44.8	139.5	43.3	183.4

partitioned into vibrational degrees of freedom. Choosing these six selected pairs of J and E_{int} allowed us to determine the dependence of the dynamics on those variables with enough trajectories at each to obtain good statistics.

The energy conservation relation for our experiments, which equates the energy of the incident photon and ensemble averaged internal vibrational energy of the parent molecule (assumed to be at thermal equilibrium with the nozzle temperature but with the assumption that rotational degrees of freedom are cooled in the supersonic expansion) to the energy distribution in the electronic, vibrational, and rotational degrees of freedom, contains several values that do not change regardless of the recoil translational energy chosen. The energy of the photon, $h\nu$, is 148 kcal mol^{-1}, the average precursor vibrational energy above zero point is approximately 2.5 kcal mol^{-1}, the bond energy of the C−Br bond is approximately 71 kcal mol^{-1}, and the departing bromine atom is assumed to be in its ground spin−orbit state, $E(^2Br_{3/2})$ = 0.0 kcal mol^{-1} for our inputs (experimentally, the Br atom is formed in it first excited spin−orbit state ∼20% of the time; however, we assume the ground state for simplicity). The remaining initial conditions can be seen in Table 1.

Velocities corresponding to vibrational motion were microcanonically sampled and scaled to the proper internal energy, adding zero-point energy of 36.1 kcal/mol to the E_{int} in Table 1. The orthogonal rotational degrees of freedom corresponding to instantaneous rotation were determined by $\vec{J} = \vec{r} \times \mu\vec{\nu}_{rel}$ from the experimentally measured translational energy distribution and the parent molecule's equilibrium geometry. The initial angular momentum is related to the rotation axis by the molecule's inertia tensor. From here, the instantaneous tangential component of the angular velocity is determined, in the center of mass reference frame, by the cross-product of the angular velocity with each atom's position:

$$\vec{\nu}_T = \vec{\omega} \times \vec{r} \tag{1.2}$$

A series of 5000 trajectories were run for each set of initial conditions including one set of 6000 trajectories where the angular momentum was explicitly removed for comparison purposes. Each was propagated using a standard velocity−verlet integration scheme, with a time step of 5 au, for approximately 12 ps or until the distance between any two atoms exceeded 12 Bohr radii. Trajectories violating conservation of energy by a significant fraction (approximately 1 kcal mol^{-1}) were discarded (although the vast majority of simulations conserved energy well), and the angular momentum was tracked throughout with the system conserving J to within 1 au.

c. Sketch Map and IRC. The sketch-map procedure has been outlined in detail and applied to many diverse systems previously so only a short summary will be provided.[31−33] The method is related to multidimensional scaling (MDS); it generates a map from a high-dimensional representation of the atomic configurations (represented with upper case coordinates in the following section) to a much lower dimensional space (represented with lower case coordinates in the following section). The lower dimensional space is much easier to visualize and interpret. A set of representative high-dimensional geometries $\{X_i\}$ (landmarks) are selected, and their low-dimensional projections $\{x_i\}$ are optimized in such a way that the Euclidian distances, $r_{ij} = r_i - r_j$, match as well as possible the distances between the corresponding high-dimensional landmarks $R_{ij} = R_i - R_j$. In practice this operation involves the iterative minimization of an objective function of the form

dx.doi.org/10.1021/jp407913t | J. Phys. Chem. A 2013, 117, 10951−10963

$$\chi^2 = \sum_{i \neq j} [R_{ij} - r_{ij}]^2 \tag{1.3}$$

Sketch map differs from conventional MDS in that the distances R_{ij} and r_{ij}, in the high- and the low-dimensional representations, respectively, are transformed by sigmoid "filter" functions using eq 1.4 and eq 1.5:

$$F(R) = 1 - (1 + (2^{A/B} - 1)(R/\sigma)^A)^{-B/A} \tag{1.4}$$

$$f(r) = 1 - (1 + (2^{a/b} - 1)(r/\sigma)^a)^{-b/a} \tag{1.5}$$

Thus, the modified objective function

$$\chi^2 = \sum_{i \neq j} [F(R_{ij}) - f(r_{ij})]^2 \tag{1.6}$$

used for the iterative minimization procedure aims at guaranteeing that landmarks which are closer together than the threshold σ will be projected close to each other and that vice versa pairs of landmarks which are farther apart than σ will be mapped to far apart projections. This is a much easier task than the distance matching procedure inherent in metric MDS. Once a set of landmarks and their projections have been obtained, it is possible to perform an out-of-sample embedding procedure that takes any atomic configuration, represented as a high-dimensional point, and maps it to the lower dimension space using the landmarks and their projections as references.[32]

When using sketch map, it is always advantageous to start from a high-dimensional description of the system that takes into account the most obvious symmetries, and the fundamental physical features of the problem at hand. In this case, for instance, we did not use the Cartesian coordinates of the atoms as the initial representation, but we associated to each atomic structure a 10-dimensional vector of coordination numbers. For selected pairs of atoms in the CD_2CD_2OH molecule (e.g., C−O, O−H, O−D, and C−D, etc.), the distance between the atoms was computed and transformed by a sigmoid function that yielded a value of one when the pair of atoms was chemically bound and a value of zero when the bond was clearly cleaved, interpolating smoothly between these extremes for intermediate, stretched configurations of the bond.

From the set of 10-dimensional vectors corresponding to the configurations visited in the various trajectories, 250 landmarks were selected with a min−max procedure[31] and were then mapped to 2 dimensions using the sketch-map algorithm, using sigmoid functions with the parameters $\sigma = 0.5$, $A = B = b = 4$, and $a = 1$. The parameter σ was chosen to be large enough to ignore vibrational motion in a locally bound region of the potential energy surface but small enough to differentiate between geometries en route to other local minima or product asymptotes. In addition to using the sketch-map procedure, the transition states and IRCs for all dissociation pathways were projected in sketch-map variables and plotted on top of the sketch-map landmark geometries. Further details are given in the Supporting Information.

RESULTS AND DISCUSSION

a. Predicting the $P(E)_T$ for OH + C_2D_4 Dissociation. The experimental translational energy distribution for the secondary dissociation leading to OH + deuterated ethene is given in Figure 4. The distribution peaks at approximately 8−9 kcal mol^{-1} and shows a long tail that extends to roughly 35 kcal mol^{-1}. The main feature peaks far from 0 kcal mol^{-1} not

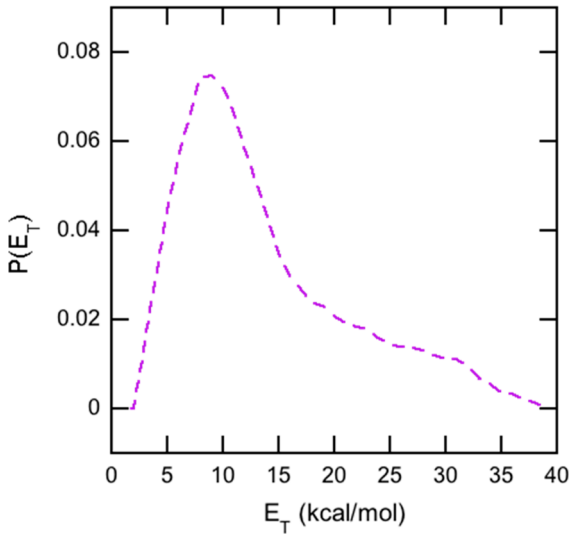

Figure 4. (Purple line) Experimentally determined translational energy distribution for CD_2CD_2OH forming OH + ethene. The distribution peaks at approximately 9 kcal mol^{-1} and displays a long-range tail that goes to zero at 35 kcal mol^{-1}. Some of the high-energy tail may result from multiphoton dissociation from the precursor.

because there are repulsive forces along the reaction coordinate leading toward OH + ethene but because the dissociating CD_2CD_2OH adduct has high angular momentum imparted to it when formed photolytically from the brominated precursor. The tangential velocity in the nascent rotating radical adduct results in the high relative velocity measured between the OH + ethene fragments. In order to attempt to predict the translational energy distribution imparted to these two fragments using the calculated distribution of angular momenta in the nascent radicals, we ran 5000 trajectories corresponding to radicals generated from the Tt conformer of the parent molecule with 29 kcal mol^{-1} of translational energy and 127 atomic units in angular momentum. For comparison, we also ran 6000 trajectories with no angular momentum but with vibrational energy of 39.2 kcal mol^{-1} matching that of the Tt conformer with E_T = 29 kcal mol^{-1}.

The resulting theoretically predicted translational energy distributions for the high angular momentum and zero angular momentum cases can be seen in Figure 5. The J = 127 au distribution is shown in solid circles and peaks near 9 kcal mol^{-1}, while the J = 0 au distribution is shown in open circles and peaks near 2 kcal mol^{-1}. One can readily see that the high angular momentum distribution more closely matches the experimental $P(E_T)$ for the majority of the distribution from 0 to 15 kcal mol^{-1} but is still slightly underfit on the fast edge. However, the experimental distribution is convolved over various conformations of the precursor, and each dissociating radical can have any number of angular momenta depending on the translational energy of the departing bromine atom relative to the radical. Most likely the high kinetic energy shoulder on the experimental $P(E_T)$ is due to multiphoton product channels contributing to the experimental spectrum. There may also be some contribution from high angular momenta imparted to the radical, but theoretical predictions will not be able to match experiment since we did not execute trajectories corresponding to the extremes of the angular momentum distributions.

It should be noted that a significant fraction of the OH and ethene fragments used to predict the distribution did not have

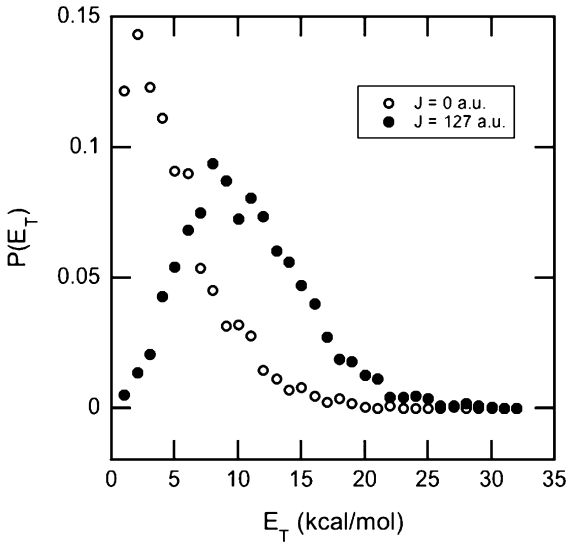

Figure 5. Two theoretically predicted $P(E_T)$s. The filled circles show the J = 127 au distribution for those radicals formed from the Tt conformation of the parent molecule, 2-bromoethanol-d_4. The open circles show the prediction for the radicals formed with no angular momentum. The $P(E_T)$ predicted from the J = 127 radicals matches the experimentally derived distribution shown in Figure 4 much better than the prediction from the J = 0 radicals.

the necessary minimum zero-point energy. Originally, the fragments were required to have proper zero-point energy; however, the $P(E_T)$ distributions were virtually unchanged when this condition was relaxed. Therefore, in order to predict the distribution with better precision, we have chosen not to discard those trajectories that violate zero-point energy for this analysis.

b. Lifetimes and Rate Constants of CD_2CD_2OH Disappearance. One of the most surprising results from this study was how quickly the trajectories dissociated for high angular momentum cases relative to those with zero. With J = 127 au, roughly 65% of all trajectories dissociated within 12 ps; however, with J = 0 au and the same amount of internal energy in vibration at the equilibrium geometry of the radical, only about 35% of those trajectories dissociated in the same time frame. This increased reaction rate upon introduction of rotational energy comes from rovibrational coupling. In a classical view, as the molecule explores the potential energy surface, its geometry (and therefore its inertia tensor) changes drastically. Under the condition that the molecule experiences no external torques, the angular momentum must remain constant; thus, the changing inertia tensor greatly affects the rotational energy of the molecule. The changing energy is either borrowed from or stored in the vibrational degrees of freedom. Therefore, in a sense, the rotational energy serves as a storehouse for additional vibrational energy that the molecule can use to surmount various reaction barriers as it proceeds along a specific intrinsic reaction coordinate.

According to statistical rate theories, the unimolecular decomposition of CD_2CD_2OH should follow first-order kinetics given by

$$N(t) = N_{tot}e^{-t/\tau} \tag{2.1}$$

The number of molecules left after time, t, denoted as $N(t)$, can also be expressed as an integral over the distribution of dissociated radicals as a function of time (eq 2.2), known as $P(t)$.

$$N(t) = N_{tot} - \int_0^t P(t')\,dt' \tag{2.2}$$

Using these two relations and binning the distribution of dissociated trajectories with respect to time, one can use nonlinear regression methods in order to determine τ, the lifetime associated with each initial condition. (In the fits, we let $N_{tot.}$ adjust to just under 5000 or 6000, respectively, to exclude the small number of directly dissociating trajectories observed at very short times.) The lifetime is inversely related to the rate constant, both of which are reported in Table 2 for each of our initial conditions.

The lifetimes range from 14.9 ps for those radicals generated with high vibrational energy from the Tt conformer to 47.1 ps for radicals created from the Gg conformer of the parent having low vibrational energy. As expected, the reaction rate increases as the energy partitioned into the vibrational degrees of freedom of the radical increases. To facilitate comparison of the data sets, we also generated initial conditions corresponding to the Tt conformer with E_{int} = 59.0 kcal mol^{-1} and J = 127 au from which we then explicitly removed the angular momentum. In this way we could generate two sets of initial conditions which differ only in angular momentum. Surprisingly, the rate constant for J = 127 au was over twice as large ($k_{J=127}$ = 6.72 × 10^{10} s^{-1}) as the J = 0 au case ($k_{J=0}$ = 3.18 × 10^{10} s^{-1}). The plots used to determine these values can be seen in Figure 6 for the Tt conformers and in Figure 7 for the Gg conformers. The plot starting at 6000 trajectories corresponds to the no rotation case and has the same initial internal vibrational energy as the J = 127 au case. All other plots have varying internal energies and angular momenta; therefore, a direct comparison with the no rotation simulation should not be made.

c. Product Branching. It should be restated that the potential energy surface is currently unable to reproduce experimentally determined branching ratios. (While the experimental results give roughly an 75−80% branching to OH + ethene with the remainder divided between H + ethenol, methyl + formaldehyde, and vinyl + water, the J = 127, E_{int} = 50.8 kcal mol^{-1} trajectories run for 12 ps gave a branching fraction of 99% to OH + ethene. [Note: Evidence for a very tiny branching to HD + vinoxy-d_3 products is given in the Supporting Information.]) This is most likely due to the use of B3LYP/cc-pVDZ for large portions of the surface. Although the

Table 2. Rates and Lifetimes for the Two Conformers and Three Translational Energies Including the No Rotation Result

	Tt conformer			Gg conformer			no rotation		
E_T (kcal mol^{-1})	τ (ps)	$N_{tot.}$	rate constant (s^{-1})	τ (ps)	$N_{tot.}$	rate constant (s^{-1})	τ (ps)	$N_{tot.}$	rate constant (s^{-1})
29.0	14.9	4827	6.72 × 10^{10}	22.0	4908	4.53 × 10^{10}	31.5	5816	3.18 × 10^{10}
32.0	21.0	4825	4.76 × 10^{10}	34.2	4918	2.92 × 10^{10}			
35.0	28.4	4860	3.52 × 10^{10}	47.1	4919	2.12 × 10^{10}			

dx.doi.org/10.1021/jp407913t | J. Phys. Chem. A 2013, 117, 10951−10963

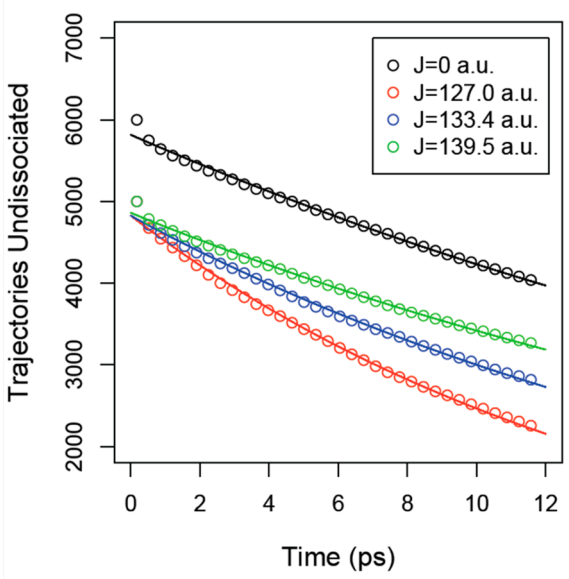

Figure 6. Plot of the number of trajectories left undissociated vs time in order to determine the first-order rate constants for the dissociation of CD_2CD_2OH, fully separating to form hydroxyl radical and ethene. The trajectories are for radicals from the Tt conformer of the parent. All four sets of initial conditions have different internal energies and different angular momenta imparted from the initial photodissociation event (see Table 1). The trajectory data (open circles) are fit (solid line) with the model described in the text, with the best fit given by the lifetimes and $N(t=0)$ in Table 2. The black circles show the no rotation case with the same internal vibrational energy at the radical's equilibrium geometry as the J = 127 au data shown in red, but no energy in rotation. The red and green circles show the trajectory data for radicals with 133.4 au and 139.5 au of angular momenta, respectively. Given the same vibrational energy at equilibrium geometry, the dissociation rate for radicals with high angular momentum is much faster than the J = 0 au simulations.

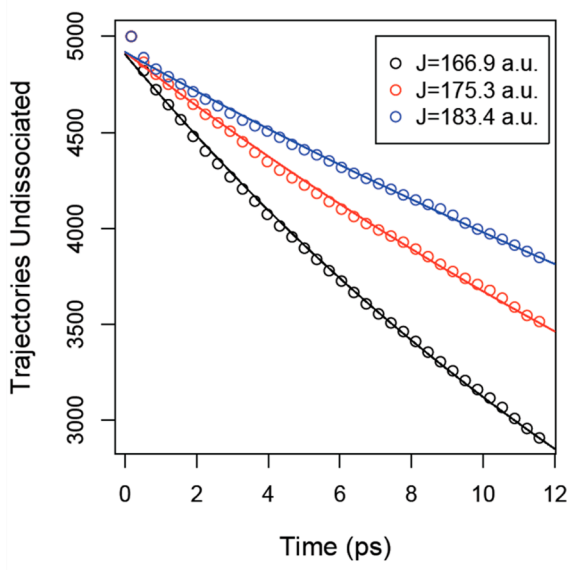

Figure 7. Number of trajectories, associated with radicals from the Gg conformer of the parent, which did not dissociate vs time. All three sets of initial conditions have different internal energies and different angular momenta imparted from the initial photodissociation event (see Table 1). The trajectory data (open circles) are fit (solid line) with the model described in the text, with the best fit given by the lifetimes and $N(t = 0)$ in Table 2

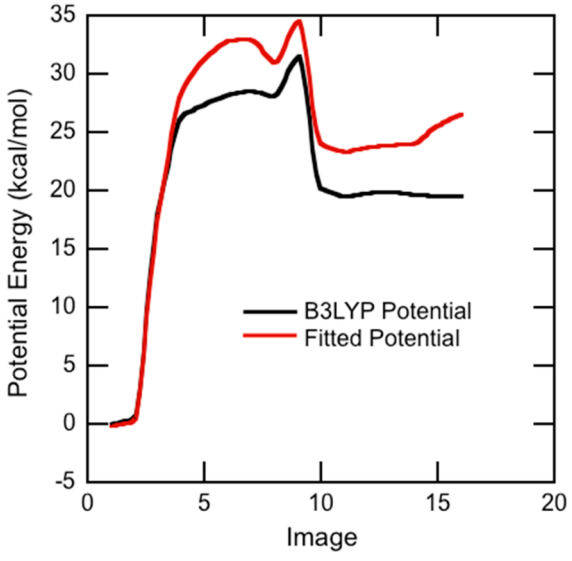

Figure 8. Plot of the potential energy surface corresponding to the lower energy transition path from the CD_2CD_2OH minimum to HOD + C_2D_3, where the zero of energy is defined as the lowest energy from the B3LYP calculations. Sixteen images from a nudged-elastic-band calculation performed at BLYP level of theory were used as input for both the B3LYP (shown in black) and fitted (shown in red) potential energy calculations. While the two surfaces match near the minimum (corresponding to image 1), the two differ greatly as the OH fragment begins to move away and abstract a D atom with energetic differences as large as 7 kcal mol^{-1} (see Supporting Information for the NEB images).

stationary points were calculated at a higher level of theory (CCSD/cc-pVDZ), the majority of the surface was still calculated at a lower level. While this results in improved energetics near minima and transition states, the surface is still dominated by the density functional theory calculations, and the potential used throughout the investigation reflects this fact.

A nudged-elastic-band[43−45] calculation was performed using 20 representative geometries from a reactive trajectory in order to determine the minimum energy path at the BLYP level of theory. The energetics of these geometries were recalculated at the B3LYP/6-311++G(3df,2p) level and checked against the fitted potential surface. Figure 8 shows the global fitted potential in red and the corresponding B3LYP calculations in black. The two calculations are nearly identical in the vicinity of the CD_2CD_2OH minimum (see Supporting Information for full details). However, as the molecule nears the transition state, differences of greater than 4 kcal mol^{-1} are observed, vastly changing the relative energetics between the reactant and product states. The B3LYP/6-311++G(3df,2p) energies are nearly 8 kcal mol^{-1} lower than those from the fitted surface for the asymptotic C_2D_3 + HOD product state. The fitted surface seems to match high-quality G4//B3LYP/6-311++G(3df,2p) calculations better than simple B3LYP calculations. The main takeaway point from this analysis is to note the difficulty of characterizing the potential surface during bond breaking, especially en route to the H atom abstraction transition state. The energies were recalculated at CCSD/cc-pVDZ, and, in this region, the norm of the T1 vector is above 0.02 indicating that there is a large degree of multireference character in the molecular process;[46] therefore, multideterminantal methods

dx.doi.org/10.1021/jp407913t | J. Phys. Chem. A 2013, 117, 10951−10963

such as CASPT2 must be used in order to accurately capture the dynamics.

Figure 2 shows the calculated intrinsic reaction coordinates (IRC) at the B3LPY/6-311++G(3df, 2p) level of theory for both the hydroxyl loss and water loss product channels. The black curve shows the energies calculated at this level of electronic structure theory with no added rotational energy, the J = 0 au case, while the red and blue curves represent the centrifugally corrected potentials for radicals produced from the Tt and Gg conformers of 2-bromoethanol-d_4, respectively. The relative difference between the OH loss and D atom abstraction transition states is roughly 5 kcal mol^{-1} for J = 0 au; however, this difference shrinks to approximately 3 kcal mol^{-1} when one accounts for the difference in rotational energy of radicals from these conformers in the transition-state regions. This should increase the importance of the abstraction channel if the available energy above the now-centrifugally corrected barriers is still substantial, thus showing the effect that angular momentum can have on product branching. However in the experiment the total available energy is fixed, so although the centrifugally corrected potentials have more similar barrier heights, the available energy is reduced and one cannot infer that branching to the abstraction channel would necessarily increase. The same geometries along the IRC were used and the potential energy was calculated for all molecular geometries from the fitted potential. Similar centrifugal corrections for the Tt and Gg conformers were added to the IRCs and compared to the original B3LYP calculations. The difference between the hydrogen abstraction and hydroxyl loss transition states shrank by 2.5 kcal mol^{-1} for both the fitted potential and the B3LYP potential; however, the fitted potential was much higher in overall energy compared to the CD_2CD_2OH minimum. Figure 9 is a comparison to Figure 2 with the same color and marker coding, except the energies reported in Figure 9 were calculated using the fitted potential surface of Kamarchik et al. employed in the quasiclassical trajectories study presented. The majority of trajectories simply dissociated to form OH + ethene (~99%) while the remaining 1% was split almost evenly among the remaining product channels with slight preference for D + ethenol.

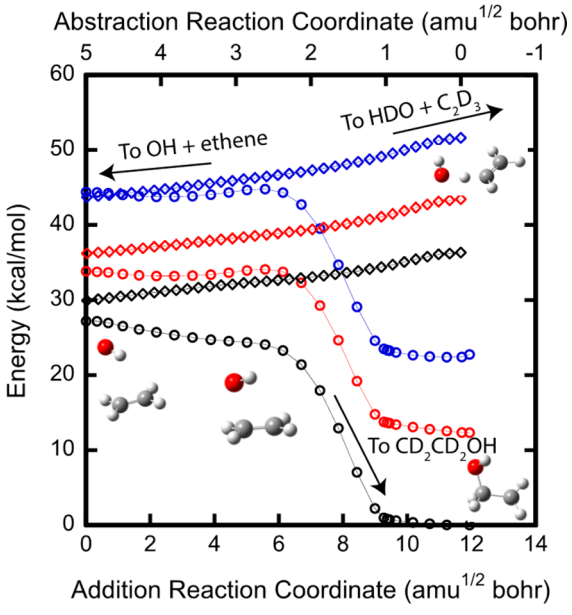

Figure 9. Comparison plot with Figure 2 showing the difference between the potential energy surface employed for trajectory calculations (this figure) and that of simple B3LYP (Figure 2). The most interesting quality of the plots is the drastic change in relative energetics between the OH loss and D-atom abstraction channels, showing the fitted surface is very different from that of the B3LYP calculations.

d. Mechanism to HOD Loss. Elucidating the mechanism to vinyl plus water has proven to be complicated. Several attempts were originally made to find a concerted water loss transition state at the B3LYP/6-311++G(3df,2pd) level of theory that may explain this result. The transition state was recently calculated and is shown to abstract a hydrogen atom from the radical carbon (as seen in Figure 10). First, the C−C−O angle contracts bringing the oxygen in close proximity to one of the deuterium atoms. The C−O bond then extends, and the vinyl radical fragment begins to flatten as the abstracted hydrogen begins to form a new bond with oxygen. This zero-point corrected barrier from CD_2CD_2OH to this concerted water loss transition state is ~74 kcal mol^{-1} at G4//B3LYP/6-311++G(3df,2pd), which is well outside the experimental parameters; the most energetic radicals only have ~50 kcal mol^{-1} of internal energy.

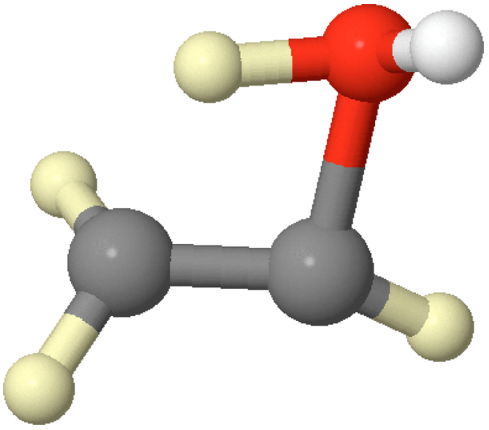

Figure 10. Energetically inaccessible transition-state structure corresponding to concerted water loss along the only IRC from CD_2CD_2OH to HOD + vinyl, calculated at B3LYP/6-311++G(3df, 2pd). The C−O bond is elongated, the C−D bond is almost completely broken, and the remaining C_2D_3 moiety is clearly starting to flatten in preparation for the new π system stabilizing the radical electron. The transition state pictured is approximately 74 kcal mol^{-1} above the CD_2CD_2OH minimum.

One looks instead to non-IRC dynamics to access the bimolecular abstraction transition state from the radical adduct. The potential energy surface shows a slight depression after hydroxyl radical loss, corresponding to a slightly stabilized hydrogen bonded complex whereby the hydrogen atom on the hydroxyl radical is loosely bound to the π-cloud on ethene. The portion of the potential surface sampled by the system en route to dissociation to OH + ethene is relatively flat, allowing the two fragments to explore a large number of orientations relative to each other. If the translational energy between the two fragments is large, the hydroxyl moiety will be virtually unaffected by the flat PES and will simply dissociate fully. If the translational energy is sufficiently low, however, this flat section of the surface can frustrate the dissociation, and, in this flat region, the OH radical has two options: the hydroxyl radical

dx.doi.org/10.1021/jp407913t | J. Phys. Chem. A 2013, 117, 10951−10963

can add via an almost barrierless reaction back to ethene re-forming the initial CD_2CD_2OH radical, or it can abstract one of the four equivalent deuterium atoms on the ethene to form HOD + vinyl-d_3. While most of the leaving OH radicals in this study had the necessary translational energy to dissociate to OH + ethene, a small portion of them formed HOD + C_2D_3 (with an unknown number that simply added back to the double bond). We were not able to assess the importance of the small van der Waals well along the OH + ethene IRC on these dynamics.

In an attempt to understand the complex motions that lead to this channel, several dimensionality reduction techniques were applied to the trajectories of interest with varying degrees of success. Sketch map proved to be the most successful and insightful of the techniques we tried. The sketch-map projections of 250 landmarks obtained from five representative trajectories—one for each product channel we considered—can be seen in Figure 11. Since the coordinates of the projections obtained with this method cannot be associated with physical coordinates in a straightforward manner, we superimposed on the map in Figure 11 the out-of-sample embedding of a few representative trajectories and the projections of the IRCs (dashed lines) and of the transition states (open circles).

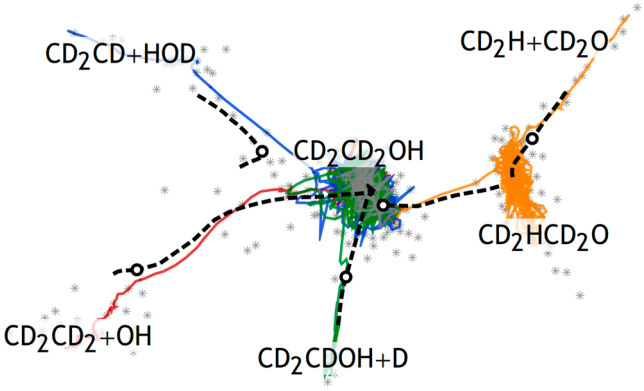

Figure 11. Sketch map of the C_2D_4OH potential surface. The map was constructed by creating a low-dimensionality representation of the 24 Cartesian coordinates that is translationally and rotationally invariant; the new representation is then reduced to sketch-map variables. The red line represents a trajectory leading to OH + CD_2CD_2; the orange isomerization, CHD_2CD_2O and subsequent dissociation to CD_2H + CD_2O; the blue, HOD + C_2D_3; the green, CD_2CDOH + D; and the gray, no reaction. The black open-face circles show the location of the transition states, and the black dashed lines, the intrinsic reaction coordinates for the isomerization and dissociation pathways.

This representation demonstrates that sketch map is capable of separating clearly the different reaction channels, giving a concise visual representation of the dissociation pathways of CD_2CD_2OH. Furthermore, visualizing IRCs using sketch map helps to extract physical insight when the trajectories are similarly mapped; one can see how much dynamical trajectories deviate from the minimum energy path, and—as we will discuss in more detail below—one can see that trajectories leading to OH + CD_2CD_2 and to HOD + C_2D_3 branch out after having visited initially a very similar set of configurations.

As described previously, many attempts were made to find a low-lying transition state that might explain such high branching to the water channel. However, most transition state finding algorithms employ steepest-descent methods that have trouble with reaction paths that bifurcate in phase space. As our pathway of interest initially follows the same reaction path as hydroxyl radical loss before the dynamics turn to abstract a deuterium atom, it is possible that our system has such a bifurcation. In such a case, the only HOD + vinyl loss transition state that could initially be located with Hessian based IRC methods might be the traditional one along the OH + ethene to HOD + vinyl IRC if the path to the CD_2CD_2OH is less steep than the abstraction TS. However, on the basis of exoergicities alone, one would have expected the path from the abstraction transition state to CD_2CD_2OH to have a steeper descent than the one to OH + ethene, so it is unlikely that we have missed an HOD + vinyl IRC resulting from a simple bifurcation.

The three plots used to elucidate the dynamics of the actual pathway leading to HOD + vinyl from the CD_2CD_2OH dissociation can be seen in Figure 12. The top plot shows five representative trajectories reduced to values in sketch map and colored according to the distance between the hydroxyl carbon and the oxygen, the middle plot shows the same five trajectories but colored according to the interatomic distance between the

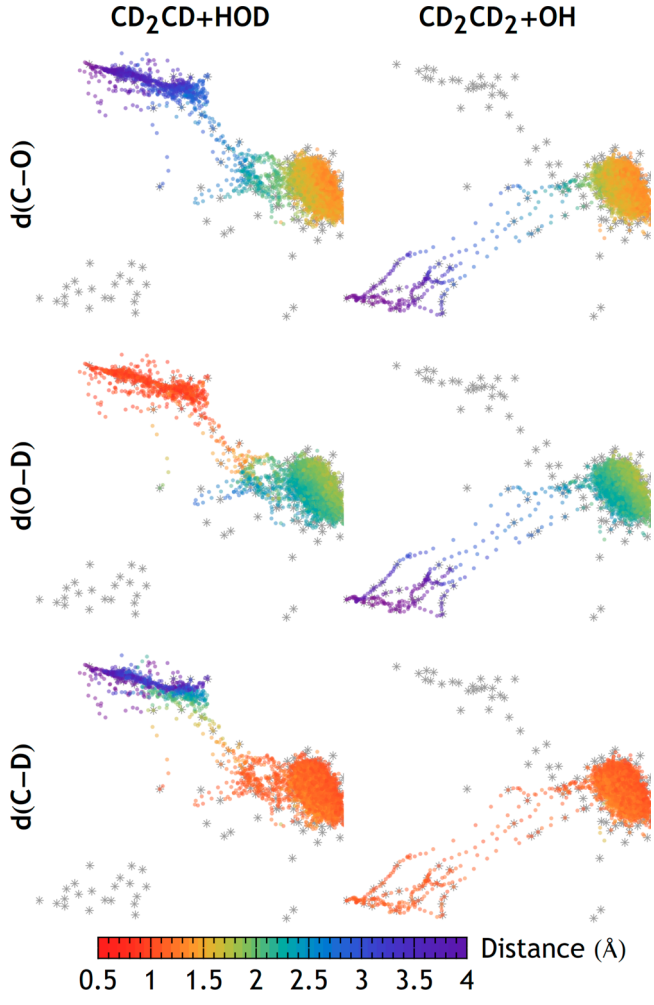

Figure 12. Trajectories plotted in sketch-map variables that dissociated to form (left) water plus vinyl and (right) OH + ethene. The data points are colored according to various interatomic distances in angstroms. The top row corresponds to the carbon oxygen distance; the middle row, the oxygen-abstracted deuterium distance; and the bottom row, the carbon deuterium distance.

dx.doi.org/10.1021/jp407913t | J. Phys. Chem. A 2013, 117, 10951−10963

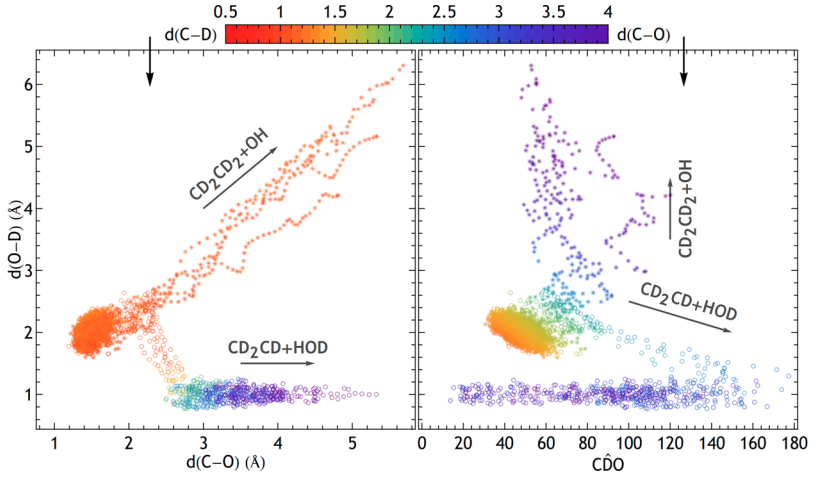

Figure 13. Bifurcation of trajectories en route to OH + ethene. The left frame plots the carbon−oxygen distance versus the oxygen-abstracted deuterium distance, colored according to the C−D distance. At a carbon−oxygen distance and an oxygen−deuterium distance of 2.0−2.5 Å, the reaction path bifurcates. The right frame plots the oxygen-abstracted deuterium distance against the carbon-abstracted deuterium−oxygen bond angle with the points colored according to the carbon−oxygen bond distance. The bond angle at a C−O distance of 2.0−2.5 Å plays a significant role in driving the bifurcation as those with small bond angles preferentially branch to the hydroxyl + ethene channel, while those with large bond angles branch to the vinyl + water product state.

hydroxyl carbon and the abstracted deuterium atom, and the bottom plot is colored according to the distance between the hydroxyl carbon and the hydrogen atom bound to oxygen. Since each point in the sketch-map representation corresponds to a particular molecular configuration, the three plots can be directly compared. Therefore, it can easily be seen that the first step en route to HOD + vinyl must be elongation of the carbon−oxygen bond. Shortly thereafter, the distance between the oxygen and abstracted deuterium atom shortens, which indicates that water loss is preferred to hydroxyl radical dissociation if the oxygen atom happens to pass near one of the four deuterium atoms. After the O−D distance has shortened significantly, the same deuterium atom finally separates fully from the carbon atom leaving HOD and C_2D_3. It seems from this analysis that one determining factor separating HOD loss from OH loss is simply proximity of a deuterium atom to the passing oxygen, as long as the OH has left with sufficiently low relative velocity to linger close to the ethene moiety and abstract a D atom. In Figure 13, we show the carbon−oxygen distance plotted against the oxygen-abstracted deuterium distance, colored according to the C−D distance (left frame), and the C−D−O bond angle versus the O−D distance with the points colored according to the C−O distance (right frame). At approximate C−O and O−D distances of 2.0−2.5 Å, the reaction path bifurcates, seemingly controlled by the C−D−O bond angle, with large angles preferentially branching to vinyl plus water. This interesting bifurcation leads the dynamics toward the linear C−D−O geometry of the abstraction transition state calculated along the OH + ethene → HOD + vinyl reaction coordinate, though most trajectories do not reach a collinear geometry. Thus, the mechanism for D atom abstraction by the departing OH is related to the OH + C_2D_4 abstraction transition state, but the dynamics samples that region of the potential energy surface differently when the trajectories start at the vibrationally excited radical intermediate.

In the prior quasiclassical trajectory study of this system, Kamarchik et al.[20] were able to roughly characterize the internal energy distribution for J = 0 au trajectories of the departing vinyl fragment by listing the fraction of radicals produced with quantum number greater than zero. It was found that the low-frequency bending modes were more likely to be excited than the high-frequency stretching modes. Our similar plot, Figure 14, shows that the high angular momentum has little effect on

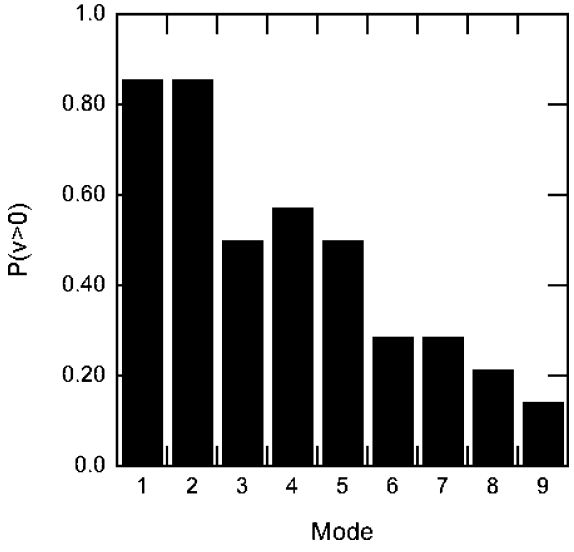

Figure 14. Percentage of trajectories formed with at least one quanta of vibrational excitation above ZPE. In ref 20, Kamarchik et al. reported the vibrational energy partitioning across the nine normal modes of vinyl radical. Notice the low-energy bending modes (namely, ν = 1, 2) are more likely to be formed in an excited vibrational state while the higher energy stretching modes (ν = 6−9) are less likely.

the vinyl product state vibrational energy distribution with the low-lying bending modes more heavily excited than the high-frequency stretching modes. In comparison to Kamarchik's results which showed roughly equal probability for the first six normal modes (ν_1−ν_6) being formed in a vibrationally excited state with the remaining three modes (ν_7−ν_9) having much smaller probability of excitation, our results show that vinyl radical is very likely to be formed in a vibrationally excited state of the first two modes with diminishing probability for the remaining seven when high angular momentum is considered.

dx.doi.org/10.1021/jp407913t | J. Phys. Chem. A 2013, 117, 10951−10963

Unfortunately, we were only able to recover a small number of simulations ending in the vinyl + water product channel; therefore, the results are not adequate enough to run statistical analysis. However, it can clearly be seen that the dissociated vinyl fragment is likely to have the lower energy modes excited versus the high-energy ones.

CONCLUSION

We have undertaken a multiyear long investigation of the main addition adduct of the bimolecular collision between hydroxyl radical and deuterated ethene, CD_2CD_2OH. Using a combination of velocity map imaging and crossed-laser molecular beam scattering experiments, we concluded that upon photodissociation of the brominated precursor the nascent radicals with sufficient internal energy dissociated to form water plus vinyl radical approximately 20% of the time, in direct disagreement with RRKM predictions. In 2010, Kamarchik et al. undertook a theoretical investigation of the corresponding hydrogenated radical by constructing the global PES and using quasiclassical trajectories. After 20 000 trajectories, they reported a modest branching to the channel of interest (approximately 1%), which they attributed to an unexpected roaming pathway.

We have performed a similar investigation using the same fitted PES of Kamarchik et al. We applied our impulsive model for rotational energy partitioning, explicitly examining the effects of high angular momentum on the product branching and dissociation dynamics. Using the two most stable conformers of the parent geometry, the Tt and Gg conformations, and the experimentally derived translational energy distribution, three angular momenta were determined for each and used as inputs in atomistic simulations. Although the branching to water plus vinyl was not able to be matched, some interesting insight into the effects of rotation was garnered. Chiefly, the added energy in rotational motion, typically assumed in simple models to be "unusable" to surmount transition barriers, has increased the rate of dissociation versus the case with no angular momentum. This interesting result is most likely attributed to rovibrational coupling, as the relevant dissociation transition states conserve angular momentum but in doing so have less energy in rotation. At present, however, the fitted PES is not able to reproduce the experimental branching ratios.

We applied the sketch-map dimensionality reduction technique in order to back out mechanistic information leading to the water + vinyl product channel. By plotting the IRCs and transition states on the projections of the landmark geometries and coloring all trajectories dissociating to water plus vinyl according to particular interatomic distances, we were able to conclude that the mechanism proceeds via a bimolecular collision-like lowest energy pathway. First, the OH moiety starts to separate from the C_2D_4 fragment elongating the C−O bond until a flat portion of the potential surface is reached. Following, the distance between oxygen and one of the four equivalent deuterium atoms on ethene is shortened, and finally the soon-to-be-broken C−D bond elongates, thus terminating at water and vinyl radical. The bifurcation of the trajectories between these two product asymptotes is correlated with the C−D−O bond angle in the critical portion of the dynamics.

In this investigation, we have been able to provide validation of our impulsive model by comparing the theoretically predicted $P(E_T)$ for the J = 0 au and J = 127 au cases for CD_2CD_2OH forming OH + C_2D_4 to the experimentally derived distribution. However, in order to provide adequate validation, more research is required. Similarly, the experimental branching fraction of roughly 20% to the water + vinyl product channel was not reproduced in this study; the surface would need to be greatly improved to provide adequate branching ratios, which would require substantial computational cost. Although the source of the large contribution from the water + vinyl product channel is still unresolved, the present study yields substantial insight into the rotational energy partitioning of the nascent radicals and the mechanism leading to the water + vinyl products observed experimentally.

ASSOCIATED CONTENT

Supporting Information

Details on the sketch-map analysis, the J distributions, the nudged elastic band images used for Figure 8, and the minor HD + vinoxy-d_3 product channel. This material is available free of charge via the Internet at http://pubs.acs.org.

AUTHOR INFORMATION

Corresponding Author

*E-mail: l-butler@uchicago.edu. Phone: 773-702-7206.

Notes

The authors declare no competing financial interest.

ACKNOWLEDGMENTS

This work was supported by the Chemical Sciences, Geosciences and Biosciences Division, Office of Basic Energy Sciences, Office of Science, U.S. Department of Energy, under Grants DE-FG02-92ER14305 (L.J.B.), DE-FG02-97ER14782 (J.M.B), and DE-AC04-94-AL85000 (E.K.) and by the EU Marie Curie IEF No. PIEF-GA-2010-272402 (M.C.).

REFERENCES

(1) Tully, F. P. Hydrogen-atom Abstraction from Alkenes by OH, Ethene and 1-Butene. *Chem. Phys. Lett.* **1988**, *143*, 510−514.

(2) Vakhtin, A. B.; Murphy, J. E.; Leone, S. R. Low-Temperature Kinetics of Reactions of OH Radical with Ethene, Propene, and 1-Butene. *J. Phys. Chem. A* **2003**, *107*, 10055−10062.

(3) Cool, T. A.; Nakajima, K.; Mostefaoui, T. A.; Qi, F.; McIlroy, A.; Westmoreland, P. R.; Law, M. E.; Poisson, L.; Peterka, D. S.; Ahmed, M. Selective Detection of Isomers with Photoionization Mass Spectrometry for Studies of Hydrocarbon Flame Chemistry. *J. Chem. Phys.* **2003**, *119*, 8356−8365.

(4) Taatjes, C. A.; Hansen, N.; McIlroy, A.; Miller, J. A.; Senosiain, J. P.; Klippenstein, S. J.; Qi, F.; Sheng, L.; Zhang, Y.; Cool, T. A.; et al. Enols Are Common Intermediates in Hydrocarbon Oxidation. *Science* **2005**, *308*, 1887−1889.

(5) Smith, I. W. M.; Zellner, R. Rate Measurements of Reactions of OH by Resonance Absorption. Park 2.-Reactions of OH with CO, C_2H_4, and C_2H_2. *J. Chem. Soc., Faraday Trans. 2* **1973**, *69*, 1617−1627.

(6) Atkinson, R.; Aschmann, S. M.; Winer, A. M.; Pitts, J. N. Rate Constants for the Reaction of OH Radicals with a Series of Alkanes and Alkenes at 299 ± 2 K. *Int. J. Chem. Kinet.* **1982**, *14*, 507−516.

(7) Atkinson, R.; Aschmann, S. M. J. N. Rate Constants for the Reaction of OH Radicals with a Series of Alkenes and Dialkenes at 295 ± 1 K. *Int. J. Chem. Kinet.* **1984**, *16*, 1175−1186.

(8) Tully, F. P. Laser Photolysis/Laser-Induced Fluorescence Study of the Reaction of Hydroxyl Radical with Ethylene. *Chem. Phys. Lett.* **1983**, *96*, 148−153.

(9) Bott, J. F.; Cohen, N. A Shock Tube Study of the Reactions of the Hydroxyl Radical with Several Combustion Species. *Int. J. Chem. Kinet.* **1991**, *23*, 1075−1094.

(10) Chuong, B.; Stevens, P. S. Kinetic Study of the OH + Isoprene and OH + Ethylene Reactions between 2 and 6 Torr and over the

Temperature Range 300−423 K. *J. Phys. Chem. A* **2000**, *104*, 5230−5237.
(11) Hippler, H.; Viskolcz, B. Addition Complex Formation *vs.* Direct Abstraction in the OH + C_2H_4 Reaction. *Phys. Chem. Chem. Phys.* **2000**, *2*, 3591−3596.
(12) Senosiain, J. P.; Klippenstein, S. J.; Miller, J. A. Reaction of Ethylene with Hydroxyl Radicals: A Theoretical Study. *J. Phys. Chem. A* **2006**, *110*, 6960−6970.
(13) Zhu, R. S.; Park, J.; Lin, M. C. Ab Initio Kinetic Study on the Low-Energy Paths of the HO + C_2H_4 Reaction. *Chem. Phys. Lett.* **2005**, *408*, 25−30.
(14) Sosa, C.; Schlegel, H. B. An ab Initio Study of the Reaction Pathways for OH + C_2H_4 → $HOCH_2CH_2$ → Products. *J. Am. Chem. Soc.* **1987**, *109*, 7007−7015.
(15) Sosa, C.; Schlegel, H. B. Calculated Barrier Heights for OH + C_2H_2 and OH + C_2H_4 Using Unrestricted Moeller−Plesset Perturbation Theory with Spin Annihilation. *J. Am. Chem. Soc.* **1987**, *109*, 4193−4198.
(16) Ratliff, B. J.; Womack, C. C.; Tang, X. N.; Landau, W. M.; Butler, L. J.; Szpunar, D. E. Modeling the Rovibrationally Excited C_2H_4OH Radicals from the Photodissociation of 2-Bromoethanol at 193 nm. *J. Phys. Chem. A* **2010**, *114*, 4934−4945.
(17) Ratliff, B. J.; Alligood, B. W.; Butler, L. J.; Lee, S.-H.; Lin, J. J. Product Branching from the CH_2CH_2OH Radical Intermediate of the OH + Ethene Reaction. *J. Phys. Chem. A* **2011**, *115*, 9097−9110.
(18) Womack, C. C.; Booth, R. S.; Brynteson, M. D.; Butler, L. J.; Szpunar, D. E. Characterizing the Rovibrational Distribution of CD_2CD_2OH Radicals Produced via the Photodissociation of 2-Bromoethanol-d_4. *J. Phys. Chem. A* **2011**, *115*, 14559−14569.
(19) Womack, C. C.; Ratliff, B. J.; Butler, L. J; Lee, S.-H.; Lin, J. J. Photoproduct Channels from $BrCD_2CD_2OH$ at 193 nm and the HDO + Vinyl Products from the CD_2CD_2OH Radical Intermediate. *J. Phys. Chem. A* **2012**, *116*, 6394−6407.
(20) Kamarchik, E.; Koziol, L.; Reisler, H.; Bowman, J. M.; Krylov, A. I. Roaming Pathway Leading to Unexpected Water + Vinyl Products in C_2H_4OH Dissociation. *J. Phys. Chem. Lett.* **2010**, *1*, 3058−3065.
(21) Townsend, D.; Lahankar, S. A.; Lee, S. K.; Chambreau, S. D.; Suits, A. G.; Zhang, X.; Rheinecker, J.; Harding, L. B.; Bowman, J. M. The Roaming Atom: Straying from the Reaction Path in Formaldehyde Decomposition. *Science* **2004**, *306*, 1158−1161.
(22) Harding, L. B.; Georgievskii, Y.; Klippenstein, S. J. Roaming Radical Kinetics in the Decomposition of Acetaldehyde. *J. Phys. Chem. A* **2009**, *114*, 765−777.
(23) Sivaramakrishnan, R.; Michael, J. V.; Wagner, A. F.; Dawes, R.; Jasper, A. W.; Harding, L. B.; Georgievskii, Y.; Klippenstein, S. J. Roaming radicals in the thermal decomposition of dimethyl ether: Experiment and theory. *Combust. Flame* **2011**, *158*, 618−632.
(24) Tenenbaum, J. B.; de Silva, V.; Langford, J. C. A Global Geometric Framework for Nonlinear Dimensionality Reduction. *Science* **2000**, *290*, 2319−2323.
(25) Balasubramanian, M.; Schwartz, E. L. The Isomap Algorithm and Topological Stability. *Science* **2002**, *295*, No. 7.
(26) Cox, T. F.; Cox, M. A. A. *Multidimensional Scaling*; Chapman and Hall: London, U.K., 1994.
(27) Coifman, R. R.; Lafon, S.; Lee, A. B.; Nadler, B.; Warner, F.; Zucker, S. W. Geometric Diffusions as a Tool for Harmonic Analysis and Structure Definition of Data: Diffusion Maps. *Proc. Natl. Acad. Sci. U. S. A.* **2005**, *102*, 7426−7431.
(28) Coifman, R. R.; Lagon, S. Diffusion Maps. *Appl. Comput. Harmonic Anal.* **2006**, *21*, 5−30.
(29) Nadler, B.; Lafon, S.; Coifman, R. R.; Kevrekidis, I. G. Diffusion Maps, Spectral Clustering and Reaction Coordinates of Dynamical Systems. *Appl. Comput. Harmonic Anal.* **2006**, *21*, 113−127.
(30) Rohrdanz, M. A.; Zheng, W.; Maggioni, M.; Clementi, C. Determination of Reaction Coordinates via Locally Scaled Diffusion Map. *J. Chem. Phys.* **2011**, *134*, No. 124116.
(31) Ceriotti, M.; Tribello, G. A.; Parrinello, M. Simplifying the Representation of Complex Free-Energy Landscapes Using Sketch-map. *Proc. Natl. Acad. Sci. U. S. A.* **2011**, *108*, 13023−13028.
(32) Tribello, G. A.; Ceriotti, M.; Parrinello, M. Using Sketch-Map Coordinates to Analyze and Bias Molecular Dynamics Simulations. *Proc. Natl. Acad. Sci. U. S. A.* **2012**, *109*, 5196−5201.
(33) Ceriotti, M.; Tribello, G. A.; Parrinello, M. Demonstrating the Transferability and the Descriptive Power of Sketch-Map. *J. Chem. Theory Comput.* **2013**, *9*, 1521−1532.
(34) Womack, C. C.; Fang, W. H.; Straus, D. B.; Butler, L. J. Assessing an Impulsive Model for Rotational Energy Partitioning to Acetyl Radicals from the Photodissociation of Acetyl Chloride at 235 nm. *J. Phys. Chem. A* **2010**, *114*, 13005−13010.
(35) North, S. W.; Blank, D. A.; Gezelter, J. D.; Longfellow, C. A.; Lee, Y. T. Evidence for Stepwise Dissociation Dynamics in Acetone at 248 and 193 nm. *J. Chem. Phys.* **1995**, *102*, 4447−4460.
(36) Riley, S. J.; Wilson, K. R. Excited Fragments from Excited Molecules: Energy Partitioning in the Photodissociation of Alkyl Iodides. *Faraday Discuss. Chem. Soc.* **1972**, *53*, 132−146.
(37) Busch, G. E.; Wilson, K. R. Triatomic Photofragment Spectra. I. Energy Partitioning in NO_2 Photodissociation. *J. Chem. Phys.* **1972**, *56*, 3626−3638.
(38) Holdy, K. E.; Klotz, L. C.; Wilson, K. R. Molecular Dynamics of Photodissociation: Quasidiatomic Model for ICN. *J. Chem. Phys.* **1970**, *52*, 4588−4599.
(39) Braams, B. J.; Bowman, J. M. Permutationally Invariant Potential Energy Surfaces in High Dimensionality. *Int. Rev. Phys. Chem.* **2009**, *28*, 577−606.
(40) Jin, Z.; Braams, B. J.; Bowman, J. M. An ab Initio Based Global Potential Energy Surface Describing CH_5^+ → CH_3^+ + H_2. *J. Phys. Chem. A* **2006**, *110*, 1569−1574.
(41) Zhang, X.; Zou, S.; Harding, L. B.; Bowman, J. M. A Global ab Initio Potential Energy Surface for Formaldehyde. *J. Phys. Chem. A* **2004**, *108*, 8980−8986.
(42) Xie, Z.; Braams, B. J.; Bowman, J. M. *Ab Initio* Global Potential-Energy Surface for H_5^+ → H_3^+ + H_2. *J. Chem. Phys.* **2005**, *122*, 224307.
(43) Jónsson, H.; Mills, G.; Jacobsen, K. W. *Classical and Quantum Dynamics in Condensed Phase Simulations*; World Scientific: Hackensack, NJ, USA, 1994; pp 385−404.
(44) Henkelman, G.; Jónsson, H. Improved Tangent Estimate in the Nudged Elastic Band Method for Finding Minimum Energy Paths and Saddle Points. *J. Chem. Phys.* **2000**, *113*, 9978−9985.
(45) Henkelman, G.; Uberuaga, B. P.; Jonsson, H. A Climbing Image Nudged Elastic Band Method for Finding Saddle Points and Minimum Energy Paths. *J. Chem. Phys.* **2000**, *113*, 9901−9904.
(46) Lee, T. J.; Taylor, P. R. A Diagnostic for Determining the Quality of Single-Reference Electron Correlation Methods. *Int. J. Quantum Chem.* **1989**, *36*, 199−207.